Numerical Investigation on Hydrodynamic Load Redistribution and Localized Clogging Characteristics of Seawater Intake Drum Screens

Seong Min Park[a*], Tae Gang Lee[b], Jae Jun Jeong[b]

[a]*Korea Hydro & Nuclear Power Co., Ltd.*
[b] *School of Mechanical Engineering, Pusan National University (PNU)*
[*]*Corresponding author: ppppsm0216@khnp.co.kr*

***Keywords :** Drum screen, Computational fluid dynamics, Porous media, Load transfer phenomenon

1. Introduction

Nuclear Power Plants (NPPs) continuously draw vast amounts of seawater to condense steam in the secondary system. As illustrated in Fig. 1, the seawater intake system of Hanul Unit 1 (FRA900) consists of coarse bar screens (1st filtration step), sluice gates, travelling screens (2nd filtration step), and drum screens (final fine filtration step), located directly upstream of the Circulating water pump (CWP) suction pits [1]. Seawater enters from both the left and right outer boundaries of the drum, passes through the fine wire mesh into the drum interior, and then flows downstream through a semicircular concrete pit into the pump suction conduits [2].

As the final fine filtration barrier in the seawater intake system, the drum screen plays a critical role in preventing marine organisms and debris from entering downstream circulating water pumps and condenser tube bundles. Its reliable operation is crucial for maintaining plant thermal efficiency and ensuring the operational continuity of the nuclear power plant. The geometry of the drum screen is shown in Fig. 2, and its main design parameters are summarized in Table I. The drum screen itself is a large cylindrical rotating structure with an outer diameter of 12 m and an effective width of 7.8 m. During normal operation, the drum screen rotates at a low speed of 2.5 m/min to continuously lift caught debris to the top, where high-pressure wash water sprays remove the debris into discharge troughs. If the differential pressure across the screen reaches 10 mbar, the operating logic switches the rotation to high speed (10 m/min) to accelerate cleaning. If the differential pressure exceeds 50 mbar (corresponding to a water level drop of $\Delta h \approx 500$ mm), the downstream CWPs are automatically tripped to prevent condenser vacuum loss and structural deformation.

As the plant continuously draws seawater, various marine organisms (e.g., jellyfish, salps, shrimp) and debris enter the intake structure, frequently causing mesh blockage and leading to power deratings or forced plant trips. Hanul Nuclear Power Plant Unit 1 alone accounts for 25 out of 28 total marine organism-related events across Korean NPPs between 1988 and 2026 [3]. In actual operation, marine organisms accumulate non-uniformly depending on localized flow velocity and intake geometry. This non-uniform blockage causes local velocity spikes, adverse pressure gradients, flow separation, and uneven structural fatigue. Furthermore, localized mesh obstruction bypasses the incoming flow, triggering progressive hydrodynamic load redistribution across the screen. Understanding this localized clogging behavior is therefore essential for stable plant operation. This behavior is monitored through the water level difference across the screen (Δh), which is maintained at approximately 15.2 mm under normal operation but can rise to about 500 mm at the emergency pump-trip condition as the wire mesh becomes clogged.

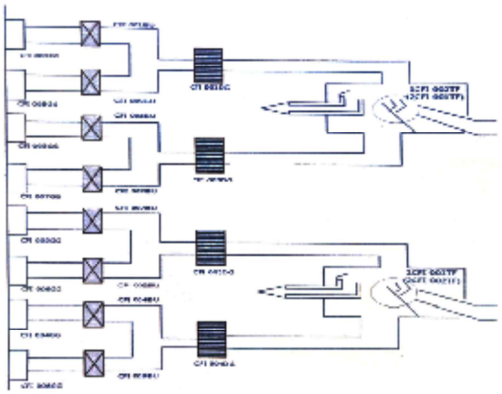


Fig. 1. Hanul NPP Unit 1 water intake system schematic.

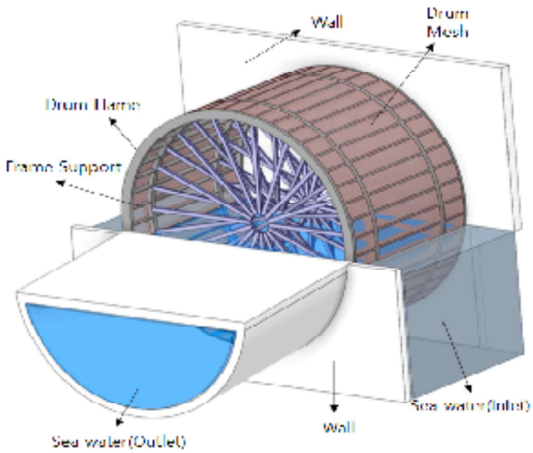


Fig. 2. Drum screen.

Table I: Drum screen parameters.

Parameter	value	unit
Drum outer diameter	12.0	m
Drum width	7.8	m
Wire diameter (D_w)	0.8	mm
Mesh opening (W)	3.0×3.0	mm
Mesh pitch (L)	3.8	mm
Volume porosity (ε)	0.835	-
Drum screen thickness	430	mm
Normal rotation speed	2.5	m/min

Previous CFD studies [4] mostly represented screen fouling as a spatially uniform loss of permeability over the entire screen — that is, a single averaged flow resistance applied across the whole mesh, rather than a resolved, position-dependent blockage. However, such an approach may not fully capture the complex 3D internal flow fields, local recirculation zones, and localized mesh blockage behaviors that develop in actual operation.

To address these limitations, this study establishes a 3D analysis model using the commercial CFD code ANSYS Fluent 2021 R2, coupled with the volume of fluid (VOF) model and a porous-media approach. The drum screen mesh is modeled as an equivalent porous medium with an equivalent numerical porosity (ε_{eff}) that reflects the actual design and operating conditions. Localized hydrodynamic loads are then analyzed under normal operating and emergency pump-trip conditions using macro/micro-zoning. Through this approach, the study quantitatively characterizes the localized clogging behavior and elucidates the hydrodynamic load redistribution mechanism across the drum screen, thereby contributing to structural integrity and stable plant operation.

2. Drum mesh modeling via porous media

2.1 Porous media theory

Modeling millions of individual fine mesh wires directly is computationally prohibitive. To solve this, the screen region is treated as a porous domain, and the pressure drop across the screen is governed by the Darcy-Forchheimer equation, which adds an inertial resistance term proportional to velocity squared to Darcy's viscous resistance law [5]:

$$S_i = -\left(\frac{\mu}{\alpha} v_i + C_2 \frac{1}{2} \rho / v / v_i\right) \quad (1)$$

where S_i is the momentum source term, v_i is the velocity component, μ is the dynamic viscosity of seawater, ρ is the seawater density, and 1/α is the viscous resistance coefficient and C_2 is the inertial resistance coefficient.

2.2 Determination of resistance coefficients

In packed beds or porous structures, viscous ($1/\alpha$) and inertial (C_2) resistance coefficients are typically determined using the theoretical Ergun equation [6]:

$$\frac{1}{\alpha} = \frac{150\,(1-\varepsilon)^2}{D_p^2\,\varepsilon^3} \quad (2)$$

$$C_2 = \frac{3.5\,(1-\varepsilon)}{D_p\,\varepsilon^3} \quad (3)$$

where ε is the volume porosity and D_p is the equivalent particle diameter. The theoretical porosity calculated from the mesh geometry (D_w = 0.8 mm, L = 3.8 mm) is:

$$\varepsilon_{theoretical} = 1 - \left(\frac{\pi \times D_w}{4 \times L}\right) \approx 0.835 \quad (4)$$

The equivalent particle diameter derived from geometric shape correction is $D_p \approx 1.118$ mm [7]. However, the standard Ergun equation assumes a 3D packed bed of spherical particles; applying it directly to a thin single-plane woven wire mesh significantly overpredicts pressure loss.

To bridge the discrepancy between theoretical packed-bed assumptions and actual field conditions (including non-ideal fouling, frame interference, and entrance angle effects), an empirical calibration factor (A) is introduced and multiplied by the theoretical porosity to define the effective (equivalent numerical) porosity, $\varepsilon_{eff} = A \times \varepsilon_{theoretical} = A \times 0.835$.

Initial baseline CFD simulations using the uncalibrated theoretical Ergun equation (A = 1.0) resulted in a water level drop of Δh = 688 mm, severely overpredicting pressure loss compared to field-measured normal operating conditions (Δh = 15.2 mm). To accurately reproduce operating conditions, the viscous (1/α) and inertial (C_2) resistance coefficients were reformulated as functions of A:

$$\frac{1}{\alpha}(A) = \frac{150\,(1-A\times 0.835)^2}{D_p^2\,(A\times 0.835)^3} \quad (5)$$

$$C_2(A) = \frac{3.5\,(1-A\times 0.835)}{D_p\,(A\times 0.835)^3} \quad (6)$$

Furthermore, to account for the numerical domain expansion of the mesh thickness (L_{real} = 1.6 mm → L_{sol} = 430 mm), a thickness scale factor $f = L_{real} / L_{sol}$ = 0.00372 was incorporated. The final resistance coefficients applied as CFD inputs in ANSYS Fluent were calculated as $1/\alpha_{final}$ (A) = $f \times 1/\alpha$ (A) and $C_{2,final}$ (A) = $f \times C_2$ (A).

Through iterative CFD calibration against field-measured normal operating water level drops (Δh = 15.2 mm), the optimal calibration factor was determined to be A = 1.193, yielding an equivalent numerical porosity of ε_{eff} = 0.996 (with $1/\alpha_{final}$ = 6.68 m^{-2} and $C_{2,final}$ = 0.045 m^{-1}). For the accident (pump-trip) condition, the calibration gives A − 1.060, ε_{eff} − 0.885 (with $1/\alpha_{final}$ = 8,526 m^{-2} and $C_{2,final}$ = 1.93 m^{-1}).

3. Numerical methodology and setup

3.1 Computational domain and mesh

To maximize computational efficiency, while preserving physical accuracy, the following model simplification strategy was adopted:

i) Symmetry Assumption: A 1/2 symmetric boundary was applied along the center plane since seawater flows symmetrically from both sides.
ii) Internal Structure Omission: Structural spokes, central shafts, and bearings were omitted because they operate below 40% of the maximum water level and do not significantly alter screen pressure drop.
iii) Effective Area Adjustment: The effective cross-sectional area was reduced by 9.8 % (67.7 m^2 → 61 m^2) to account for structural frame blockages.
iv) Rotation Omission: Drum rotation (2.5 m/min) was neglected in the steady-state analysis as its tangential speed is negligible compared to the incoming bulk water flow rate (32,000 kg/s).

The computational domain of the drum screen is shown in Fig. 3. A Poly-Hexcore hybrid meshing scheme was employed. High-quality hexahedral cells were placed in main flow passages, polyhedral cells handled complex transitional regions, and 10 layers of fine meshing were embedded within the porous domain. Grid sensitivity testing was performed across 6 cases, and the results are summarized in Table II, considering computational cost and variations in water level drop. Case 3 (605,518 nodes) was selected as the final mesh. The final mesh is shown in Fig. 4

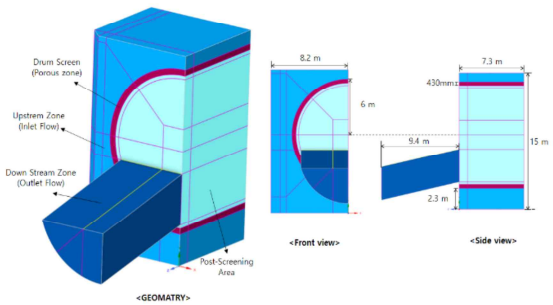


Fig. 3. Computational domain of the drum screen.

Table II: Grid sensitivity test.

Case	Nodes	Δh (mm)
Case 1	104,532	19.5
Case 2	332,104	16.3
Case 3	605,518	15.2
Case 4	932,312	15.2
Case 5	1,158,214	15.2
Case 6	1,421,183	15.2

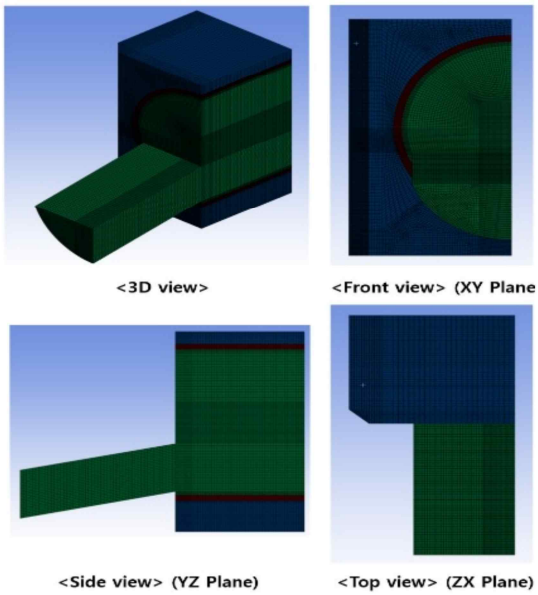


Fig. 4. Hybrid poly-hexcore mesh generation.

3.2 Boundary conditions and solver summary

Steady-state calculations were performed. The pressure-based solver was coupled with the Realizable k-ε turbulence model, which excels in predicting flow separation, streamline curvature, and recirculation eddies downstream of bluff structures. The VOF multiphase model tracked the interface between seawater and air. The specific numerical solver settings and physical input variables are summarized in Table III.

The spatial configuration and setup of the boundary conditions applied to the computational domain are illustrated in Fig. 5 [8].

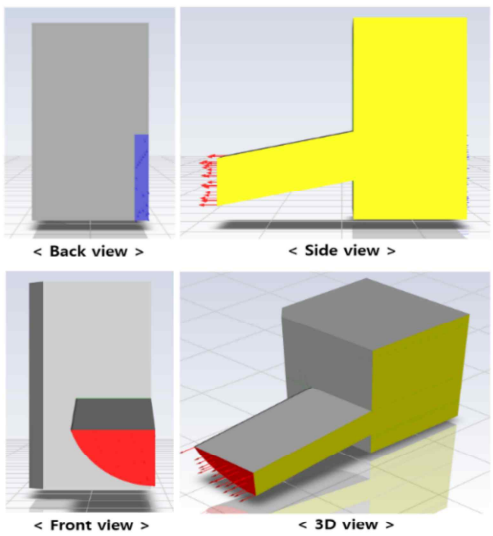


Fig. 5. Boundary condition sctup.

Table III: Solver & input variables.

Category	Parameter	Type	Value & Description
Solver setup	Solver type	Pressure-based steady state	Pseudo-transient formulation
	Multiphase model	Volume of fluid	Eulerian VOF formulation (Explicit interface tracking)
	Turbulence model	Realizable k-ε	Enhanced wall treatment, swirl correction
	Pressure-velocity coupling	Coupled	Accelerated convergence for free-surface flow
	Spatial discretization	PRESTO! (Pressure)	Specialized for steep hydrostatic gradients
		Compressive (VOF)	Sharp free-surface interface resolution
		2nd Order Upwind	Applied to momentum, k , and ε equations
Boundary conditions	Inlet	Mass flow inlet	16,000 kg/s(1/2 symmetry of the total 32,000 kg/s)
		Open channel enabled	Initial free surface water level = 6,670 mm
	Outlet	Pressure outlet	Open channel enabled; full-pipe suction flow
		Reference height	Free surface level set to 6,655 mm
	Ceiling	Pressure inlet	Air-only pressure inlet (prevents air accumulation)
	Center plane	Symmetry	1/2 symmetry boundary along central channel
	Walls	No-slip wall	Standard wall functions
Porous media setup	Porosity	Custom ('A')	0.996 (Normal) / 0.885 (Accident)
	Viscous resistance	Directional vector	6.68 m^{-2} (Normal) / 8,526 m^{-2} (Accident)
	Inertial resistance	Directional vector	0.045 m^{-1} (Normal) / 1.93 m^{-1} (Accident)

4. Results and discussion

4.1 Normal operating conditions

Under normal operation, incoming seawater maintains strong directional momentum through the narrow intake channel before entering the main drum chamber. As illustrated in the 3D streamlines in Fig. 6, The collision with the structural walls and drum frame forms large asymmetric recirculation loops and bottom vortices.

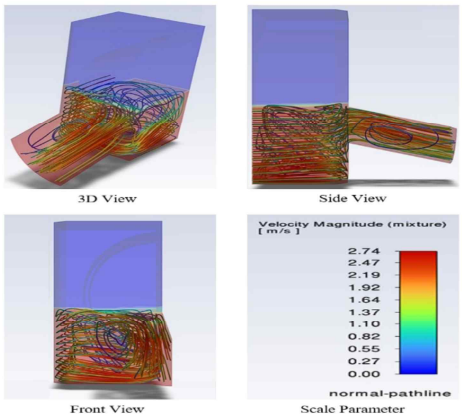


Fig. 6. 3D Streamlines under normal operating conditions.

Using the calibrated standard model (A = 1.193), the 3D flow field and pressure gradients under normal operating conditions were evaluated as follows:

i) Large recirculation and vortex formation: Seawater entering the wider drum chamber from the narrow intake conduit collides with the front boundary walls and creates strong rotational vortices and upward surge patterns near the chamber floor due to elevation differences in the outlet pipe. This induces localized flow stagnation at the lower sections of the screen.

ii) Macro and micro-zoning dynamic pressure analysis : As illustrated in Fig. 7, Macro-zoning (9-grid division) and micro-zoning (36 sub-grid division of high-load regions) were established to evaluate local hydrodynamic load distributions. The macro-zoning dynamic pressure results summarized in Table IV reveal that dynamic pressure concentrates heavily at the lower outlet side (Zones G and I). To avoid underestimating localized structural stress, the high-pressure macro-zones (D, G, II, I) were further discretized into 9 sub-zones each (36 sub-zones total). As presented in Table V, a global dynamic pressure peak of 2,045.0 Pa occurred at Zone G-1 (lower-left quadrant near the outlet). This identifies the lower-left section as the primary localized

clogging zone that initiates asymmetric hydrodynamic load concentration.

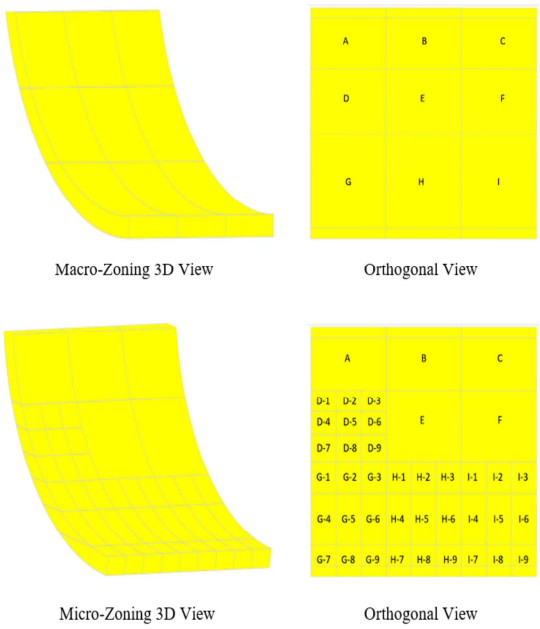


Fig. 7. Macro (9 grid) and micro zoning (36 sub-grid division of high-load regions).

Table IV: Macro-zoning dynamic pressure (Unit: Pa).

Height (Location)	Left (Outlet)	Center	Right (Inlet)
Upper	A:765.5	B:61.7	C:95.2
Middle	D:861.7	E:45.4	F:18.8
Lower	G:974.4	H:529.9	I:411.2

Table V: Micro-zoning dynamic pressure (Unit: Pa).

Height (Location)		Left (Outlet)	Center	Right (Inlet)
D	Up	1 : 1548.3	2 : 691.3	3 : 172.7
	Mid	4 : 1724.8	5 : 714.7	6 : 139.0
	Low	**7 : 1891.9**	8 : 733.7	9 : 110.4
G	Up	**1 : 2045.0**	2 : 739.5	3 : 94.8
	Mid	**4 : 2043.5**	5 : 608.5	6 : 70.6
	Low	**7 : 1639.3**	8 : 751.8	9 : 631.8
H	Up	1 : 36.7	2 : 29.6	3 : 16.7
	Mid	4 : 24.3	5 : 12.9	6 : 6.1
	Low	7 : 792.9	**8 : 940.7**	**9 : 1014.1**
I	Up	1 : 3.7	2 : 11.8	3 : 41.6
	Mid	4 : 10.1	5 : 38.9	6 : 112.3
	Low	**7 : 974.1**	8 : 739.4	9 : 367.9

4.2 Emergency shutdown conditions

To simulate the automatic pump trip limit (Δh = 500 mm), the effective porosity was drastically reduced to 0.885 (A = 1.06), representing a severe accumulation of marine debris. This restriction induced a massive water level difference of Δh = 478 mm, which is in close statistical agreement (95.6 %) with the actual plant trip point. The upstream level rises to 7,300 mm while the downstream level drops to 6,822 mm. The altered flow field and recirculation behavior under emergency shutdown conditions are illustrated in the 3D streamlines in Fig. 8.

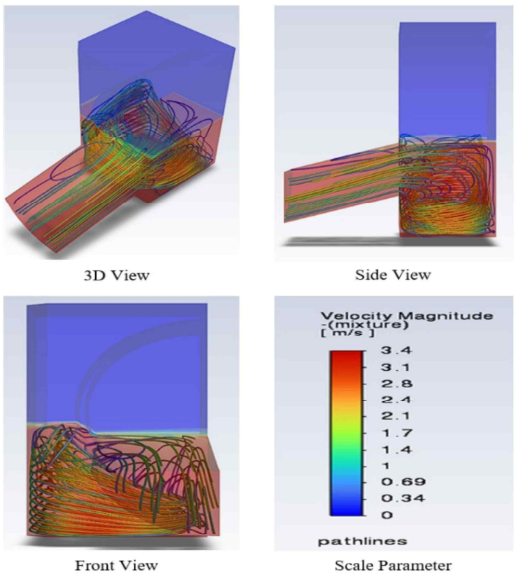


Fig. 8. 3D Streamlines under emergency shutdown conditions.

The detailed hydrodynamic characteristics under these conditions were evaluated as follows:

i) Fluid cushioning effect: As the screen blockage progresses, seawater accumulates upstream of the screen, raising the upstream level to 7,300 mm and dropping the downstream level to 6,822 mm. The high-static-pressure water cushion formed upstream absorbs the kinetic energy of incoming fluid, causing the local dynamic pressure peak at Zone G-1 to drop sharply by 90.4 % from 2,045.0 Pa to 196.8 Pa.

ii) Load transfer phenomenon: While localized kinetic impact peaks diminish, the primary stress state shifts from dynamic kinetic impact to static hydrostatic compaction. Furthermore, kinetic energy redistributes across the entire screen face and shifts toward the lower central region (Zone H-7: 739.5 Pa).

4.3 Comparison of normal and accident conditions

This section synthesizes and compares the hydrodynamic behaviors observed under normal operation and severe blockage conditions, highlighting the localized clogging characteristics and the resulting hydrodynamic load redistribution mechanism across the drum screen. A comprehensive comparison of the hydrodynamic parameters, primary load locations, and physical engineering insights across both operating regimes is summarized in Table VI.

Table VI: Summary of hydrodynamic parameters under operating conditions.

Parameter	Normal operation (A=1.193)	Emergency trip (A=1.060)	Physical shift & engineering insights
Water level drop (Δh)	16mm	478mm	Steep rise in static hydrostatic pressure
Peak dynamic pressure	2,045.0 Pa (Zone G-1)	739.5 Pa (Zone H-7)	Local peak attenuated by 90.4 % due to fluid cushioning
Primary load location	Lower-left quadrant near outlet (G-1, G-4)	Lower-center drum section (H-7, H-8, H-9)	Load center shifts from outlet wall toward central boundary
Dominant hazard mode	Localized kinetic impact & bio-fouling	Surface hydrostatic compaction	Stress mode transforms from dynamic fatigue to static compression

5. Summary and conclusions

This study developed a calibrated 3D CFD numerical model integrating the VOF multiphase model and Porous Media theory to investigate the localized clogging characteristics and hydrodynamic load redistribution of the seawater intake drum screen at Hanul Nuclear Power Plant Unit 1. The key findings are summarized below:

i) Field-validated resistance correlation: An effective porosity calibration model was established to overcome the theoretical limitations of the Ergun equation when applied to thin woven wire meshes, successfully reproducing field-measured water level drops under normal (Δh = 15.2 mm) and trip (Δh = 478 mm) conditions.

ii) Identification of high-vulnerability zones: Micro-zoning analysis under regular operation identified a dynamic pressure peak of 2,045.0 Pa concentrated at the lower outlet quadrant (Zone G-1), proving that this area experiences the highest initial risk for marine organism adhesion and localized clogging.

iii) Elucidation of load transfer mechanism: Under severe accident blockage conditions, an upstream fluid cushioning effect attenuates localized dynamic pressure peaks by over 90%, while redistributing kinetic loads toward the lower central section (Zone H-7) and rapidly increasing global hydrostatic compaction forces across the drum frame.

iv) Plant maintenance optimization: The localized clogging and load redistribution characteristics identified in this studyprovide a crucial scientific benchmark for optimizing differential water level sensor placements, deploying targeted backwash nozzle arrays at high-load zones (lower-left quadrant), and establishing proactive maintenance strategies to prevent unexpected plant deratings.

REFERENCES

[1] KORDI, "Performance Analysis of Intake Screens in Power Plants on Mass Impingement of Marine Organisms," Korea Ocean Research & Development Institute, 2006.

[2] KHNP, "Final Safety Analysis Report (FSAR) for Hanul Nuclear Power Plant Units 1 & 2," Korea Hydro & Nuclear Power Co., Ltd., 2026.

[3] KINS, "Incident and Failure Investigation Report - Manual Trip of Hanul Units 1 and 2 Turbine/Generator due to Marine Organism Inflow at Intake Structure," Korea Institute of Nuclear Safety, 2021.

[4] K - water, "CFD Analysis of the Pressure Drop caused by the Screen Blockage Rate in a Membrane Strainer," Korea Water Resources Corporation, 2024.

[5] Forchheimer, P [1901] Wasserbewegung durch Boden. Zeitschrift des vereines Deutscher Ingenieure, 45, 1782-1788

[6] S. Ergun, "Fluid flow through packed columns," Chemical Engineering Progress, Vol. 48, No. 2, pp. 89-94, 1952.

[7] R. B. Bird, W. E. Stewart, and E. N. Lightfoot, Transport Phenomena, 2nd ed., John Wiley & Sons, New York, 2002.

[8] S.M. Park, Evaluation of the performance and position-dependent effects of drum screen meshes for seawater intake at Hanul Nuclear Power Plant Unit 1 Using CFD code (Master Thesis), School of Mechanical Engineering, Pusan National University, 2026.